Single-shot visualization of evolving laser- or beam-driven plasma wakefield accelerators

Zhengyan Li, Rafal Zgadzaj, Xiaoming Wang, Yen-Yu Chang, and Michael C. Downer

Citation: AIP Conference Proceedings **1507**, 160 (2012); doi: 10.1063/1.4773689
View online: http://dx.doi.org/10.1063/1.4773689
View Table of Contents: http://scitation.aip.org/content/aip/proceeding/aipcp/1507?ver=pdfcov
Published by the AIP Publishing

Single-Shot Visualization of Evolving Laser- or Beam-Driven Plasma Wakefield Accelerators

Zhengyan Li, Rafal Zgadzaj, Xiaoming Wang, Yen-Yu Chang, Michael C. Downer

Department of Physics and Institute of Fusion Studies, University of Texas at Austin, Austin, TX, USA 78712

Abstract. We introduce Frequency-Domain Tomography (FDT) for visualizing sub-ps evolution of light-speed refractive index structures in a single shot. As a prototype demonstration, we produce single-shot tomographic movies of self-focusing, filamenting laser pulses propagating in a transparent Kerr medium. We then discuss how to adapt FDT to visualize evolving laser- or beam-driven plasma wakefields of current interest to the advanced accelerator community. For short ($L \sim 1$ cm), dense ($n_e \sim 10^{19}$ cm^{-3}) plasmas, the key challenge is broadening probe bandwidth sufficiently to resolve plasma-wavelength-size structures. For long ($L \sim 10$ to 100 cm), tenuous ($n_e \sim 10^{17}$ cm^{-3}) plasmas, probe diffraction from the evolving wake becomes the key challenge. We propose and analyze solutions to these challenges.

Keywords: frequency-Domain Tomography, frequency-domain holography, multi-object-plane holography, CT
PACS: 52.38.Kd, 41.75.Jv, 52.70.Kz

INTRODUCTION

Evolution of plasma wake structures is a key component of the function of both laser-driven [1] and electron- and proton-driven [2, 3] plasma wakefield accelerators. For example, in the "bubble" or "blowout" regime, expansion and contraction of the bubble can initiate and terminate, respectively, injection of ambient plasma electrons into the accelerator structure [4]. However, detailed knowledge of such evolution is currently available only from intensive simulations based on estimated initial conditions. In previous work, we developed frequency-domain holography (FDH) [5] to visualize quasi-static (*i.e.* non-evolving) wake structures in the laboratory in a single shot [6]. Single-shot visualization is essential for low-repetition-rate systems, and/or when shot-to-shot fluctuations are significant. FDH employs a probe that co-propagates with the light speed index structure, thereby accumulating phase shift

$$\Delta\varphi(\zeta,x) = \int_0^L \Delta n(\zeta,x,y=y_{slit},z)dz, \tag{1}$$

where ζ denotes distance behind the laser- or particle-beam driver, x and y are transverse distances from its propagation axis, z is the distance it has propagated into the plasma of length L, and y_{slit} is the lineout of the phase-modulated probe selected by the slit of a spectrometer, inside which the probe interferes with a temporally advanced reference pulse. $\Delta\varphi(\zeta,x)$ is reconstructed by Fourier-transforming the frequency-domain hologram, or interference pattern, between probe and reference pulses [5]. For linear laser wakes whose evolution over the propagation length is negligible, $\Delta\varphi(\zeta,x)$ is proportional to local plasma density variation $\Delta n(\zeta,x,y=y_{slit},z)$, and thus constitutes a "snapshot" of the wake [6]. For nonlinear bubble regime wakes at $n_e > 10^{19}$ cm^{-3}, the bubble reshapes the probe amplitude profile by refraction into an "optical bullet", which identifies the bubble's presence [7]. However, both of these measurements use a collinear geometry, and thus average over z-dependent variations, as shown in Eq. (1).

Recently, we introduced the frequency-domain streak camera in which a probe pulse propagated obliquely to the object [8]. The index structure swept across the probe's spatio-temporal profile, imprinting a phase shift streak that recorded information about the object's z-evolution. Transverse lineouts perpendicular to the streak axis are integrals, or projections, of the index structure at a specific propagation position z and projection angle ϕ. The effective projection angle ϕ is related to laboratory probe angle θ by

$$\phi = \arg\left[\frac{1}{\beta_{ob}}\left(1-\frac{\beta_{pr}}{\beta_{ob}}\cos\theta\right)+i\frac{\beta_{pr}}{\beta_{ob}}\sin\theta\right], \tag{2}$$

Advanced Accelerator Concepts
AIP Conf. Proc. 1507, 160-168 (2012); doi: 10.1063/1.4773689

where β_{pr}, β_{ob} are group velocities of probe and object, respectively, normalized to c. The streak is then a time sequence of the object's projections at angle ϕ. To recover the complete evolving structure $\Delta n(\zeta, x, z)$, one can then combine information from multiple streaks at different ϕ, as in medical computerized tomography (CT).

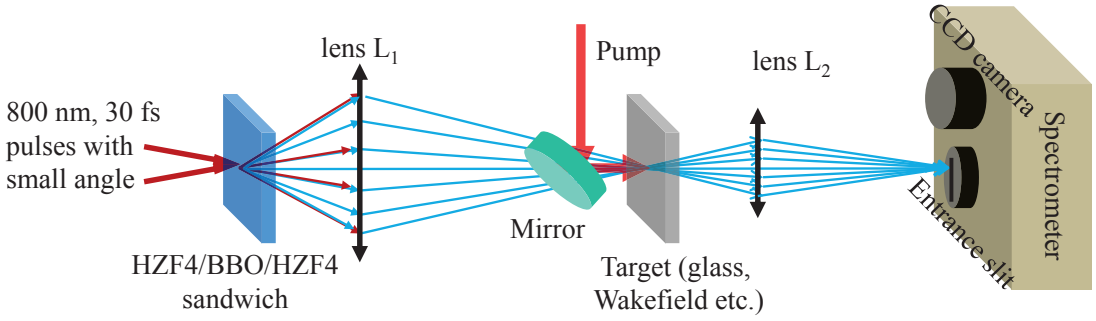

FIGURE 1. Schematic set-up for single-shot frequency domain tomographic imaging of evolving laser-generated structures.

FREQUENCY DOMAIN TOMOGRAPHY

Figure 1 shows the schematic set-up of a frequency-domain tomography experiment designed to produce a single-shot "movie" of an evolving laser-generated index structure. To prove the principle, we selected as an evolving object the nonlinear refractive index envelope $\Delta n(\zeta, x, y, z)$ surrounding a 800nm, 100 fs, micro-Joule pump pulse with peak power exceeding the critical power for self-focusing as it propagated through a transparent Kerr medium, a 3-mm-thick fused silica plate of nonlinear index $n_2 = 2 \times 10^{-16}$ cm^2/W. Several probe pulses crossed the main pulse's path at lab angles in the range $-7.6^\circ \leq \theta \leq 9.5^\circ$, corresponding to effective projection angles in the range $-65^\circ \leq \phi \leq +68^\circ$. In designing this experiment, we placed high premium on generating, detecting and processing multiple probes in a compact, cost-efficient way. As shown in Fig. 1, two 800 nm probe-generating pulses that were split from the pump generated an array of chirped, frequency-doubled probe pulses in a single step when they crossed simultaneously in an HZF4/BBO/HZF4 sandwich. In the first HZF4 glass (5 mm thick, $n_2 \sim 10^{15}$ cm^2/W), cascaded degenerate four wave mixing yielded up to eight daughter probes. Second harmonic generation and sum frequency generation in the BBO crystal further doubled the number of probes, while shifting the probe wavelength to 400 nm. The second 1.5 cm thick HZF4 glass chirped the probes to ~ 600 fs duration. A single lens L_1 directed each probe across the pump path through the sample, where each acquired a phase streak that recorded evolution of the refractive index structure from a different angle. Detection and processing of all probes was accomplished with a single spectrometer in a single-shot by angular multiplexing: lens L_2 collected and imaged all probes from the glass exit face to the entrance slit of an imaging spectrometer. Inside the spectrometer, they mutually interfere with a temporally advanced 400 nm reference pulse, creating a grid-like frequency domain interferogram (see Fig. 2(a)) on a CCD camera at the spectrometer's detection plane. Fourier transformation of this data reconstructed all phase streaks without cross-talk. Fig. 2(b) shows a typical example of a reconstructed phase streak. Tomographic reconstruction techniques [9] then produced a movie of the evolving refractive index structure from the phase streaks. Fig. 2(c) shows an example of 5 selected frames of a single-shot movie depicting the evolving index profile of a pump pulse that entered the Kerr medium at its beam waist at approximately twice the critical power. The first 3 frames show the pulse monotonically self-focusing. For the last 2 frames, corresponding to propagation through the second half of the medium, self-focusing was arrested as a self-guided filament formed. The dominant new feature that appeared here was a steep-walled index "hole" near the center of the Δn profile (last frame). Such a narrow index hole can only be explained by plasma formation. This is because six photons are needed to create an electron-hole pair in fused silica, so plasma generation scales as the sixth power of intensity I and thus occurs only in the intense center of the self-focused profile. Negative higher-order Kerr effects $(n_4 I^2 + n_6 I^3 + \cdots)$ may also be present [10, 11], but cannot create such a steep index hole because they scale as lower powers of I. Thus the FDT movie provided direct visual evidence that plasma generation was the dominant physical mechanism responsible for arresting self-focusing and forming a self-guided filament, thereby addressing a recent controversy [12, 13]. Further details of the prototype FDT procedure and experiments will be published elsewhere. In the following sections, we propose how this prototype FDT system can be modified to visualize advanced plasma-based accelerator structures of current interest to the advanced accelerator community.

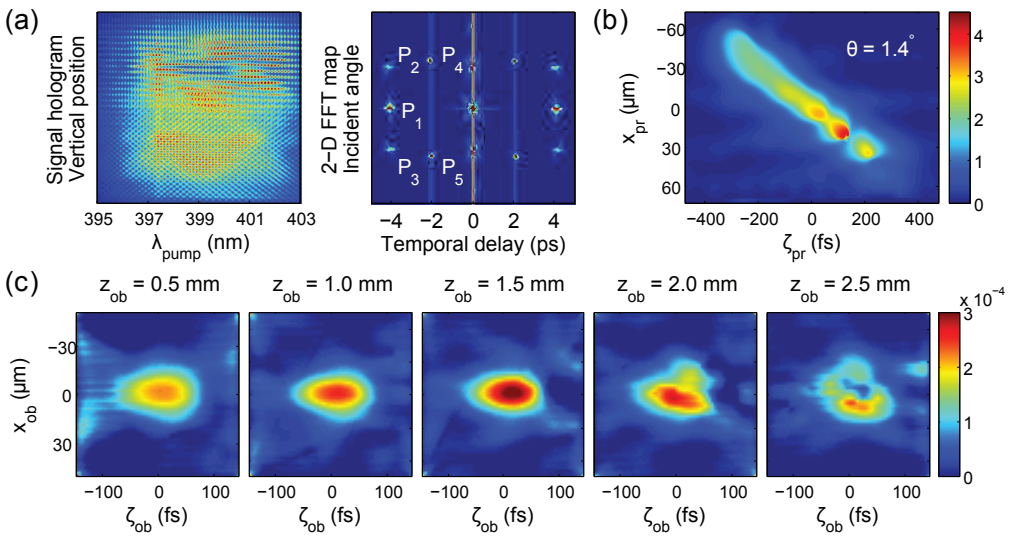

FIGURE 2. Experimental results of FDT visualization of index structures in glass. **(a)** Raw hologram (left panel) and its 2D Fourier transform map (right). **(b)** selected frequency domain streak camera (FDSC) at $\theta = 1.4°$. **(c)** Reconstructed movie frames of the index structure evolution.

VISUALIZATION OF CENTIMETER-LONG PLASMA ACCELERATORS

A typical short (mm- to cm-long) plasma wakefield accelerator producing ~ 100 MeV electrons is driven by a terawatt laser in plasma of density $n_e \sim 10^{19}$ cm^{-3}. Single-shot visualization of the dynamics of such an accelerator requires only a slight modification of the prototype FDT system described in the previous section. The two new challenges are: (1) the high density implies plasma period $T = 2\pi\sqrt{m_e\varepsilon_0/n_e e^2} \approx 35$ fs, so wider probe bandwidth ($\Delta\lambda_{pr} \sim 100$ nm) is needed than in the prototype experiment to achieve the required temporal (ζ) resolution; (2) group velocity mismatch between probe and object is smaller in plasma ($\beta_{pr} - \beta_{ob} \sim 10^{-3}$) than in glass ($\sim 10^{-2}$), so from Eq. (2), probe lab angles θ need range over only several mrad, and must be accurately controlled at that level.

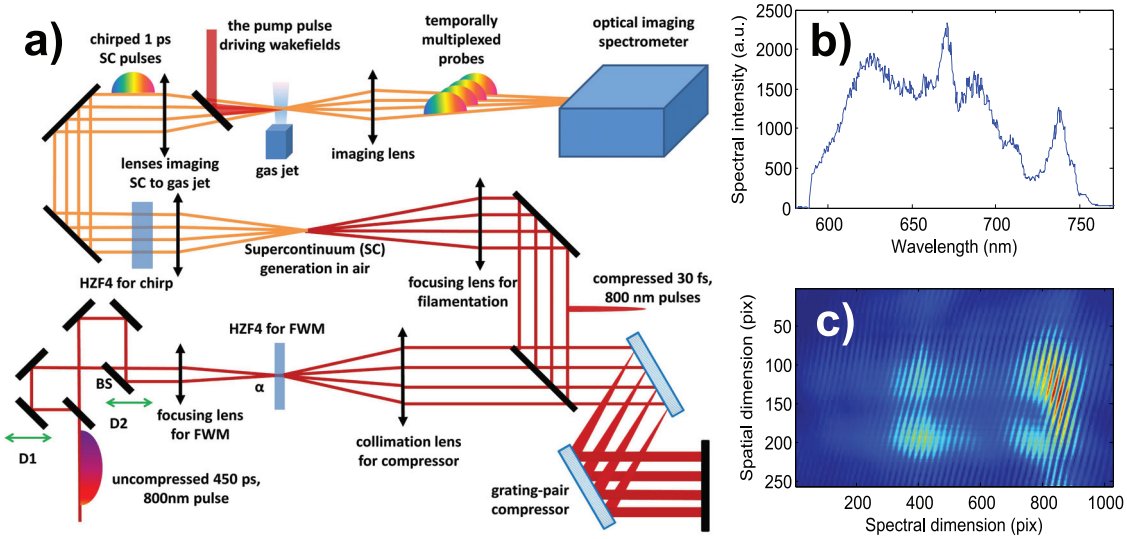

FIGURE 3. **(a)** Set-up for generating an array of broadband probe pulses needed for tomographic imaging of wakefield accelerator structures in cm-long plasmas of density $n_e \sim 10^{19}$ cm^{-3}. **(b)** Spectrum of broadband supercontinuum conical emission probes with $\Delta\lambda_{pr} \sim 100$ nm. **(c)** Frequency domain hologram of two beams with an angle and time delay between them. Fringes along wavelength dimension demonstrated temporal coherence and those along spatial dimension for spatial coherence.

Fig. 3a shows a ~ 100 nm bandwidth FDT system that we designed to meet these challenges. Supercontinuum

conical emission in air was previously used as a method for increasing probe bandwidth for spectral interferometry measurements that used only a single probe pulse [14]. Here we extended this technique to generate a temporally synchronized probe array consisting of 4 to 6 broadband mJ pulses for tomographic imaging, as illustrated in Fig. 3. A $\sim$ 10 mJ pulse was split from the uncompressed main pulse ($\tau \sim 450$ ps) and divided into two equal copies. As in the prototype experiment, they intersected in HZF4 glass to generate a probe array by cascaded four-wave mixing. A lens then collimated the array and sent it to a grating-pair compressor for compression to $\sim$ 30 fs. A lens after the compressor then focused the entire array in air sufficiently loosely ($f = 4$ m, $f\# \sim 400$) that multi-filamentation was avoided and spatial chirp minimized. Probes of bandwidth $\Delta\lambda_{pr} \sim 100$ nm were generated, as shown in Fig. 3(b). A lens then collimated the broadened probe array, an HZF4 glass plate chirped it to $\sim$ 1 ps duration, and two more lenses imaged it, first, to the interaction region, then to the same spectrometer used for the prototype experiments. Fig. 3(c) shows that both spatial and temporal coherence of the probe array is maintained when any one of the probes and the reference interfere in the spectrometer. Milli-rad level probe angle control was achieved by translating delay stage D_2 (see Fig. 3(a)) with an accuracy of $\sim 10\,\mu$m, yielding α control with uncertainty as small as 10^{-5} rad given the typical focal length of tens of centimeters. Because probe angles only one tenth of those used in the prototype FDT experiment, neighboring peaks in the reciprocal 2D hologram (Fig.2) corresponding to probes that arrive simultaneously at the spectrometer will overlap, resulting in crosstalk. To avoid this, probes are temporally multiplexed [8] — *i.e.* they arrive at the spectrometer spaced by $\sim$ 100 fs, thereby spreading their reciprocal peaks along the λ axis and avoiding overlap. This spacing is easily achieved by introducing a $\sim$ 100 fs delay between the two $\sim$ 450 ps probe-generating pulses, which does not affect their four-wave mixing efficiency, but conveniently produces a ps pulse train with 100 fs spacing after compression.

VISUALIZATION OF METER-LONG PLASMA ACCELERATORS

The next generation of plasma-based accelerators will use 0.1 to 1m-length plasma of density $n_e \sim 10^{17}$ cm^{-3} to achieve accelerating fields of $\sim$ 1 GV/cm, dephasing and pump depletion lengths of $\sim$ 1m, and electrons of multi-GeV energy. For example, the Texas Petawatt Laser-driven laser wakefield accelerator uses $\sim$ 10 cm long plasma of density $n_e \sim 4\times 10^{17}$ cm^{-3} [15], has accelerated electrons to 2 GeV [16], and is theoretically capable of producing $\sim$ 10 GeV electrons [17]. As another example, the e-beam driven accelerator at the Facility for Accelerator Science and Experimental Tests (FACET) at the Stanford Linear Accelerator is expected to increase electron energy by tens of GeV over $\sim$ 1 m of plasma of $n_e \sim 10^{17}$ cm^{-3} [18]. Over these meter-scale interaction lengths, the effect of the index object $\Delta n(\zeta, x, y = y_{slit}, z)$ on a visible or near-UV probe pulse is no longer well-described by Eq. (1), which is valid only in the geometric optics, or negligible diffraction, limit — *i.e.* when the probe wave number k, interaction length L, and object transverse size $r_\perp$ satisfy

$$kr_\perp^2 > L. \tag{3}$$

For *e.g.* $\lambda_{pr} = 400$ nm, $r_\perp \sim 10\,\mu$m, cm-scale terawatt-laser-driven accelerators ($L = 1$ cm) easily satisfy inequality (3), whereas meter-scale plasma accelerators ($L \geq 1$ m) do not. In this case, Eq. (1) must be replaced by a wave equation

$$\frac{\partial}{\partial z}A(\zeta,x,y,z) = \frac{i}{2k}\left(\frac{\partial^2}{\partial x^2}+\frac{\partial^2}{\partial y^2}\right)A(\zeta,x,y,z) + ik_0\Delta n(\zeta,x,y,z)A(\zeta,x,y,z), \tag{4}$$

where k_0 is the probe wave vector in vacuum, $k = nk_0$ is the probe wave vector in the homogeneous plasma with index $n = \sqrt{1-\omega_p^2/\omega^2}$, $A(\zeta,x,y,z)$ is the complex envelope function of the probe electrical field $E(\zeta,x,y,z) = A(\zeta,x,y,z)\exp(ikz)$ under the slow variation envelope approximation (SVEA), which is valid for the low density ($\sim 10^{17}$ cm^{-3}) plasmas used in the Texas Petawatt and FACET experiments. To connect Eq. (4) with Eq. (1), note that the first term on the right hand side of Eq. (4) describes diffraction. Neglecting this term, and taking $A(\zeta,x,y,z) = |A(\zeta,x,y)|\exp[i\Delta\phi_{pr}(\zeta,x,y,z)]$ with $z-$independent (*i.e.* non-refracting) amplitude $|A(\zeta,x,y)|$, Eq. (4) reduces straightforwardly to Eq. (1). However, when criterion (3) is not met, Eq. (4) must be retained in its entirety to describe probe pulse interaction with the index object. Avoidance of diffraction is one reason that conventional medical CT systems often use x-rays instead of visible light.

Fortunately, diffractive tomographic imaging is well developed in fields such as optical coherence tomography (OCT) [19] and seismic diffraction tomography [20] where images are extracted in highly scattering or diffractive media. In the remainder of this section, we propose an approach to wakefield imaging drawn from these fields. In the next sub-section, we solve Eq. (4) analytically with a Green function method and define a "propagator" for probes.

With this definition, probe modification integrated over a long interaction length becomes analogous to phase shift $\Delta\varphi(\zeta,x)$ integrated over short interaction length.

Solution of the probe propagation equation and the propagator

The index structure $\Delta n(\zeta,x,y,z)$ of a plasma wake modulates the probe field $A(\zeta,x,y,z)$ from its original undisturbed profile $A_i(\zeta,x,y,z)$ both in amplitude and phase. Amplitude modulation is described by a refraction factor $t(\zeta,x,y,z) = |A(\zeta,x,y,z)/A_i(\zeta,x,y,z)|$, phase modulation by a phase shift $\Delta\varphi(\zeta,x,y,z)$ similar to Eq. (1). Defining a complex phase shift $\psi(\zeta,x,y,z) = \log t(\zeta,x,y,z) + i\Delta\varphi(\zeta,x,y,z)$ that includes both of these, the phase-modulated probe field can be written $A(\zeta,x,y,z) = A_i(\zeta,x,y,z)\exp\psi(\zeta,x,y,z)$, and the index structure is encoded in the complex phase shift. It is proved in reference [21] that

$$\frac{\partial A_i\psi}{\partial z} = \frac{i}{2k}\nabla_\perp^2(A_i\psi) + ik_0A_i\left[\Delta n + \frac{(\nabla_\perp\psi)^2}{2kk_0}\right], \tag{5}$$

which, like Eq. (4), has the form of a Schrödinger wave equation. Eqs. (4) and (5) can be generalized to a Helmholtz equation $\nabla^2E + k^2E = -2k_0k\Delta nE$, which has been intensively investigated in OCT [19] and seismic diffraction tomography [20] problems. Following these studies, we define the Green function $G(\mathbf{r}-\mathbf{r}')$ of the Schrödinger equation (4), which satisfies

$$\frac{\partial}{\partial z}G(\mathbf{r}-\mathbf{r}') - \frac{i}{2k}\left(\frac{\partial^2}{\partial x^2} + \frac{\partial^2}{\partial y^2}\right)G(\mathbf{r}-\mathbf{r}') = ik_0\delta(\mathbf{r}-\mathbf{r}'), \tag{6}$$

where $\mathbf{r} = x\mathbf{e}_x + y\mathbf{e}_y + z\mathbf{e}_z$. Fourier transforming Eq. (6), we obtain the Green function

$$G(\mathbf{r}-\mathbf{r}') = \frac{kk_0}{2\pi(z-z')}\exp\frac{ik\left[(x-x')^2+(y-y')^2\right]}{2(z-z')}H(z-z'), \tag{7}$$

where $H(z-z')$ is the Heaviside step function. The complex probe phase shift can then be written

$$A_i(\zeta,\mathbf{r})\psi(\zeta,\mathbf{r}) = \int A_i(\zeta,\mathbf{r}')\left[\Delta n(\zeta,\mathbf{r}') + \frac{(\nabla_\perp\psi(\zeta,\mathbf{r}'))^2}{2kk_0}\right]G(\mathbf{r}-\mathbf{r}')d\mathbf{r}'. \tag{8}$$

To linearize Eq. (8), we introduce the Rytov approximation $2kk_0|\Delta n| \ll (\nabla_\perp\psi)^2$ [21], which leads to

$$A_i(\zeta,\mathbf{r})\psi(\zeta,\mathbf{r}) = \int A_i(\zeta,\mathbf{r}')\Delta n(\mathbf{r}')G(\mathbf{r}-\mathbf{r}')d\mathbf{r}'. \tag{9}$$

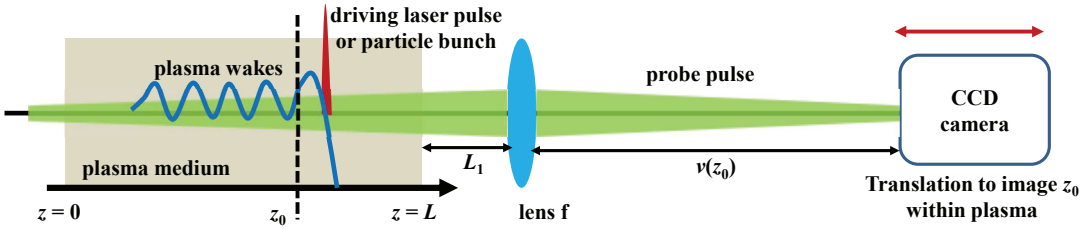

FIGURE 4. Schematic set-up for imaging a probe field interacting with an evolving laser- or beam- driven plasma wakefields from an object plane located at $z = z_0$.

Figure 4 shows a schematic set-up for imaging the evolving probe field in which a plasma medium extends from $z = 0$ to L, and a lens with focal length of f is placed a distance L_1 after its exit plane. The position of a CCD camera is adjusted to image a selected object plane at z_0. The effective object distance is thus $u(z_0) = L_1 + (L - z_0)/n$ and the effective image distance is $v(z_0) = [f^{-1} - u(z_0)^{-1}]^{-1}$. Using Eqs. (5) - (9), the field $A(\zeta,\mathbf{r}_{s\perp})$ at the CCD camera is

$$A_i\left(\zeta, -\frac{\mathbf{r}_{s\perp}u(z_0)}{v(z_0)}, z_0\right)\psi(\zeta,\mathbf{r}_{s\perp}) = \frac{k_0^2}{2\pi}\int_0^L\frac{dz}{z_0-z}\int d\mathbf{r}_\perp\exp\frac{ik[\mathbf{r}_\perp + u(z_0)\mathbf{r}_{s\perp}/v(z_0)]^2}{2(z_0-z)}\Delta n(\zeta,\mathbf{r}_\perp,z)A_i(\zeta,\mathbf{r}_\perp,z), \tag{10}$$

where $\mathbf{r}_\perp = x\mathbf{e}_x + y\mathbf{e}_y$, and $\mathbf{r}_{s\perp} = x_s\mathbf{e}_x + y_s\mathbf{e}_y$ is the corresponding vector in the image plane. We now define the "propagator" of the probe imaged from object plane z_0 to be

$$P\left(\mathbf{r}_\perp + \frac{u(z_0)\mathbf{r}_{s\perp}}{v(z_0)}, z; z_0\right) = \frac{k_0^2}{2\pi(z_0 - z)} \exp \frac{ik\left[\mathbf{r}_\perp + u(z_0)\mathbf{r}_{s\perp}/v(z_0)\right]^2}{2(z_0 - z)}. \tag{11}$$

Eq. (10) then simplifies to

$$A_i\left(\zeta, -\frac{\mathbf{r}_{s\perp}u(z_0)}{v(z_0)}, z_0\right)\psi(\zeta, \mathbf{r}_{s\perp}) = \int_0^L dz \int d\mathbf{r}_\perp P\left(\mathbf{r}_\perp + \frac{u(z_0)\mathbf{r}_{s\perp}}{v(z_0)}, z; z_0\right)\left[\Delta n(\zeta, \mathbf{r}_\perp, z) A_i(\zeta, \mathbf{r}_\perp, z)\right] \tag{12}$$

For short interactions (*i.e.* $L \ll kr_\perp^2$) and $z \sim z_0$ everywhere in the medium, the propagator reduces to a Dirac δ-function and Eq. (12) becomes

$$\psi(\zeta, x_s, y_s) = ik_0 \Delta n\left[\zeta, -x_s u(z_0)/v(z_0), -y_s u(z_0)/v(z_0), z_0\right] L \tag{13}$$

whose real part is zero, and whose imaginary part is just the accumulated phase shift given by Eq. (1) — *i.e.* the geometric optics regime. However, for long interactions, the index structure at z far from z_0 (*i.e.* $|z - z_0| \gg kr_\perp^2$) becomes blurred — *i.e.* $\langle \Delta n(\zeta, x_{s\perp}, y_{s\perp}, z)\rangle_{\mathbf{r}_\perp} = \int \mathbf{r}_\perp \Delta n(\zeta, \mathbf{r}_\perp, z)$ — and contributes to $\psi(\zeta, \mathbf{r}_{s\perp})$ through the propagator $P(\mathbf{r}_\perp + u(z_0)\mathbf{r}_{s\perp}/v(z_0), z; z_0)$, which is proportional to $|z - z_0|^{-1}$. Thus the total, integrated out-of-focus contribution scales approximately as

$$|\psi(\zeta, x_s, y_s)| \sim \left|k_0 \langle \Delta n(\zeta, x_{s\perp}, y_{s\perp}, z)\rangle_{\mathbf{r}_\perp} L\right| \frac{\ln(L/kr_\perp^2)}{L/kr_\perp^2}. \tag{14}$$

Eq. (14) implies that the maximum phase shift for long propagation is no longer determined by the product ΔnL as in FDH, but scales as $\ln L$. In addition, refraction becomes significant, so that $t(\zeta, x, y)$ couples with the phase shift $\Delta\varphi(\zeta, x, y)$, and both become important in reconstructing the index profile.

Multi-object-plane holography

The formalism of the previous sub-section described the modulated probe when imaged from a *single* object plane at z_0, as illustrated in Fig. 4. However, to de-convolve the probe's complex modification in the presence of diffraction and unravel underlying plasma wake dynamics, *multiple* object planes at z_j ($j = 1, 2, ..., N$) must be imaged, as in OCT [19]. Thus we generalize the formalism of the previous sub-section to include multiple object planes.

The 4D plasma wakefield evolution history $\Delta n(\zeta, x, y, z)$ must be reconstructed from a combination of complex phases $\psi^{(j)}(\zeta, x, y)$ derived from N cameras imaging object planes at z_j. We first convert the $\mathbf{r}_\perp$– domain Eq. (12) to the corresponding $\mathbf{k}_\perp$–domain equation:

$$\tilde{A}_i\left(\zeta, -\frac{v(z_0)\mathbf{k}_\perp}{u(z_0)}, z0\right) \otimes \tilde{\psi}(\zeta, \mathbf{k}_\perp) = \int_0^L dz' \tilde{P}\left(\frac{v(z_0)\mathbf{k}_\perp}{u(z_0)}, z; z_0\right)\left[\Delta\tilde{n}\left(\zeta, -\frac{v(z_0)\mathbf{k}_\perp}{u(z_0)}, z\right) \otimes \tilde{A}_i\left(\zeta, -\frac{v(z_0)\mathbf{k}_\perp}{u(z_0)}, z\right)\right]. \tag{15}$$

For multi-object-plane imaging with N detectors sampling equally spaced z_j — *i.e.* $|z_{j+1} - z_j| = \Delta z$ — Eq. (15) can be written in matrix form:

$$\begin{pmatrix} \tilde{A}_i(\zeta, \mathbf{k}_\perp, z_1) \otimes \tilde{\psi}^{(1)}(\zeta, -u(z_1)\mathbf{k}_\perp/v(z_1)) \\ \tilde{A}_i(\zeta, \mathbf{k}_\perp, z_2) \otimes \tilde{\psi}^{(2)}(\zeta, -u(z_2)\mathbf{k}_\perp/v(z_2)) \\ \vdots \\ \tilde{A}_i(\zeta, \mathbf{k}_\perp, z_N) \otimes \tilde{\psi}^{(N)}(\zeta, -u(z_N)\mathbf{k}_\perp/v(z_N)) \end{pmatrix} =$$

$$\begin{pmatrix} \tilde{P}(-\mathbf{k}_\perp, z_1; z_1) & \tilde{P}(-\mathbf{k}_\perp, z_2; z_1) & \cdots & \tilde{P}(-\mathbf{k}_\perp, z_N; z_1) \\ \tilde{P}(-\mathbf{k}_\perp, z_1; z_2) & \tilde{P}(-\mathbf{k}_\perp, z_2; z_2) & \cdots & \tilde{P}(-\mathbf{k}_\perp, z_N; z_2) \\ \vdots & \vdots & \ddots & \vdots \\ \tilde{P}(-\mathbf{k}_\perp, z_1; z_N) & \tilde{P}(-\mathbf{k}_\perp, z_2; z_N) & \cdots & \tilde{P}(-\mathbf{k}_\perp, z_N; z_N) \end{pmatrix} \begin{pmatrix} \Delta\tilde{n}(\zeta, \mathbf{k}_\perp, z_1) \otimes \tilde{A}_i(\zeta, \mathbf{k}_\perp, z_1) \\ \Delta\tilde{n}(\zeta, \mathbf{k}_\perp, z_2) \otimes \tilde{A}_i(\zeta, \mathbf{k}_\perp, z_2) \\ \vdots \\ \Delta\tilde{n}(\zeta, \mathbf{k}_\perp, z_N) \otimes \tilde{A}_i(\zeta, \mathbf{k}_\perp, z_N) \end{pmatrix} \Delta z \quad . \tag{16}$$

Now the plasma wake index profile $\Delta n(\zeta, x, y, z)$ can in principle be reconstructed from the measured complex phase shifts $\psi^{(j)}(\zeta, x_s, y_s)$ by taking an inverse of Eq. (16), given the propagator matrix which corrects for diffraction and

the unperturbed field profile $A_i(\zeta,x,y,z)$. Such direct transformation-based reconstruction is analogous to tomographic techniques such as filtered back-projection (FBP) based on the Radon transform [9]. Alternatively, algebraic reconstruction techniques (ART) that iteratively solve the inverse of Eq. (16) from a guessed initial solution for $\Delta n(\zeta,x,y,z)$ [9] can be used.

Practical approaches to single-shot diffractive 4D visualization

The need for multiple object planes in the diffractive regime, outlined in the previous sub-sections, applies to *each individual probe* of the evolving object $\Delta n(\zeta,x,y,z)$. In order to visualize $\Delta n(\zeta,x,y,z)$ in 4D, multiple probes propagating at different angles with respect to the object are needed, as in the FDT system of Fig. 1. To generalize this system to the diffractive regime, it would be necessary to distribute each of the phase-modulated probes after lens L_2 in Fig. 1 via beam-splitters to multiple spectrometers located at different image distances that correspond to different object distances in the range $0 < z < L$. This brute force approach unfortunately requires as many spectrometers as object planes, and can rapidly become prohibitively expensive and cumbersome.

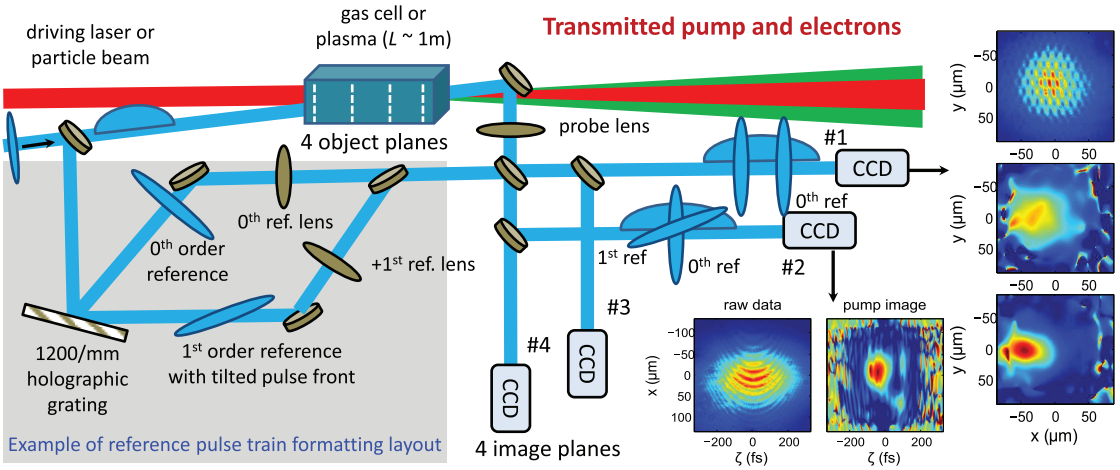

FIGURE 5. Schematic diagram of single-shot multi-object-plane holography (MOPH) designed for imaging wakes in meter-length plasma. A temporally stretched probe pulse propagates at a small angle to the plasma wake. A probe lens images the phase-modulated probe from several object planes to CCDs placed at corresponding image planes, where each copy interferes with formatted trains of compressed reference pulses, each impinging on CCD at a slightly different angle. Reference formatting layout in lower left yields reference pulse pair shown impinging on CCD 2. MOPH results for a test object created by propagating a pair of 30 fs pump pulses through fused silica are shown at right and lower right. Right: holography using the probe and two 0th order references temporally separated by 300 fs. Top panel, raw hologram; middle panel, phase shift decoded by the leading reference; bottom panel, phase shift decoded by the trailing reference. Lower right: holography using the probe and the 1st order, tilted reference. Left panel, raw hologram; right panel, reconstructed phase shift revealing spatio-temporal (ζ-x) profile of the index structure created by one of the pumps.

To avoid this expense, we propose that the modulation imprinted on individual probes should be measured without the use of spectrometers when visualizing long-interaction-length plasma wakefield accelerators. Fig. 5 schematically illustrates a spectrometer-free approach to recording the complex modulation imprinted on a representative chirped probe pulse. After the interaction, a probe lens images the probe from each of several object planes within $0 < z < L$ to each of several CCD cameras placed at corresponding image planes, using beam splitters after the probe lens to divide the probe into the necessary number of copies. Each modulated probe copy must interfere with a reference in order to recover its complex phase modulation. To avoid the use of spectrometers, we replace frequency-domain interference of the imaged probe with a single chirped reference pulse with *space-domain* interference of the imaged probe with a formatted train of wide bandwidth, fully compressed reference pulses. Each reference pulse in the train overlaps in time with a different "cut" of the temporally stretched probe, and impinges on the CCD at a slightly different angle. The resulting interference pattern can be de-convolved by 2D Fourier transformation from that of other reference pulses in the train.

To test this space-domain interference approach, we created a test object by propagated two 30 fs, 800 nm pump pulses separated by 200 fs through a 1 mm fused silica medium, thereby creating two tandem nonlinear refractive index objects. The hologram in Fig. 5 (right) resulted from interfering a temporally stretched ($\sim$ 600 fs), 400 nm probe that co-propagated with the pump pulse pair with each of two 30 fs reference pulses that impinged on CCD 1 at slightly different angles, and overlapped temporally with the probe's phase-modulated portions. The $x-y$ cuts of the two pump-induced index changes shown at the right were recovered straightforwardly in a single shot. Additional reference pulses at other time delays, impinging on CCD 1 at other angles, could be added straightforwardly to the train to recover the complete longitudinal probe profile. As a second-example, we recovered an $x-\zeta$ cut of the probe in a single shot (shown in Fig. 5, lower right) by interfering it with a 30 fs reference pulses with a tilted front (shown impinging on CCD 2), which was produced straightforwardly by 1st order diffraction from a 1800/mm holographic grating [22] (as shown in Fig. 5, lower left).

Although the approach illustrated in Fig. 5 requires multiple CCDs for each probe and complicated reference-pulse-formatting and probe-beam-splitting optics, these added items are inexpensive, and necessary for single-shot imaging in the presence of probe diffraction. Moreover, eliminating spectrometers compensates for the added cost. An added advantage of space-domain holography is that it records the object's full transverse profile, whereas the entrance slit of a spectrometer selects a lineout of the probe's 3D phase shift structure $\Delta\varphi(\zeta,x,y)$ at y_{slit}, abandoning potentially important transverse profile information for cylindrically asymmetric objects. Absence of a slit is also an advantage when imaging the phase structure of probe pulses with large shot-to-shot pointing fluctuations.

CONCLUSION

We have demonstrated frequency-domain tomography (FDT) for visualizing index structures that evolve over $\sim$mm interaction length. By broadening the probe bandwidth and applying other technical modifications, this FDT technique can be used to visualize evolving high density (10^{19} cm^{-3}) plasma wakefield accelerators over similar interaction length. For future low density (10^{17} cm^{-3}), meter-long accelerators, we propose multi-object-plane holography (MOPH), a variation of optical coherence tomography (OCT), to correct for diffraction-induced image distortion. Because multiple detectors are needed to image multiple object planes, we propose a spectrometer- and slit-free holographic approach to MOPH. In addition to avoiding the expense of multiple spectrometers, slit-free holography is less sensitive to pointing instability than spectrometer-based detection schemes, and obtains transverse and longitudinal profiles of plasma wakes simultaneously, enabling robust, quasi-4D movies of wakefield accelerator structures.

ACKNOWLEDGEMENTS

This work was supported by U. S. Department of Energy grants DE-FG03-96ER40954 and DE-FG02-07ER54945 and by NSF grant PHY-0936283.

REFERENCES

1. S. F. Martins, R. A. Fonseca, W. Lu, W. B. Mori, L. O. Silva, "Exploring laser-wakefield-accelerator regimes for near-term lasers using particle-in-cell simulation in Lorentz-boosted frames," *Nature Phys.* **6**, 311–316 (2010).
2. I. Blumenfeld, et al., "Energy doubling of 42 GeV electrons in a metre-scale plasma wakefield accelerator," *Nature* **445**, 741–744 (2007).
3. A. Caldwell, K. Lotov, A. Pukhov, F. Simon, "Proton-driven plasma-wakefield acceleration," *Nature Phys.* **5**, 363–367 (2009).
4. S. Kalmykov, S. A. Yi, V. Khudik, G. Shvets, "Electron self-injection and trapping into an evolving plasma bubble," *Phys. Rev. Lett.* **103**, 135004 (2009).
5. S. P. Le Blanc, E. W. Gaul, N. H. Matlis, A. Rundquist, M. C. Downer, "Single-shot ultrafast phase measurement by frequency domain holography," *Opt. Lett.* **25**, 764–766 (2000).
6. N. Matlis *et al.*, "Snapshots of laser wakefields," *Nature Phys.* **2**, 749–753 (2006).
7. P. Dong *et al.*, "Formation of optical bullets in laser-driven plasma bubble accelerators," *Phys. Rev. Lett.* **104**, 134801 (2010).
8. Z. Li, R. Zgadzaj, X. Wang, S. Reed, P. Dong, M. C. Downer, "Frequency-domain streak camera for ultrafast imaging of evolving light-velocity objects," *Opt. Lett.* **35**, 4087–4089 (2010).
9. G. T. Herman, "Fundamentals of computerized tomography : image reconstruction from projections,", 2nd edition, Springer, New York (2009).

10. V. Loriot, E. Hertz, O. Faucher, and B. Lavorel, "Measurement of high order Kerr refractive index of major air components," *Opt. Exp.* **17**, 13429–13434 (2009); **18**, 3011–3012 (2010).
11. K. Ekvall, C. Lundevall, and P. van der Meulen, "Studies of the fifth-order nonlinear susceptibility of ultraviolet-grade fused silica," *Opt. Lett.* **26**, 896–898 (2001).
12. Béjot, P. *et al.*, High-order Kerr Terms allow ioinization-free filamentation in gases, *Phys. Rev. Lett.* **104**, 103903 (2010).
13. Polynkin, P. *et al.*, Experimental tests of the new paradigm for laser filamentation in gases, *Phys. Rev. Lett.* **106**, 153902 (2011).
14. K. Y. Kim, I. Alexeev, H. M. Milchberg, "Single-shot supercontinuum spectral interferometry," *Appl. Phys. Lett.* **81**, 4124–4126 (2002).
15. X. Wang *et al.*, "Self-injected petawatt laser-driven plasma electron acceleration in 10^{17} cm^{-3} plasma," *J. Plasma Phys.* **78**, 413-419 (2012).
16. X. Wang *et al.*, "Self-injected petawatt laser-plasma acceleration of electrons to 2 GeV," paper in this Proceedings volume (2012).
17. S. Y. Kalmykov *et al.*, "Numerical modeling of multi-GeV laser wakefield accelerator driven by a self-guided petawatt pulse," *New Journal of Physics* **12**, 045019 (2010).
18. M. Hogan *et al.*, "Plasma wakefield acceleration experiments at FACET," *New. J. Phys.* **12**, 055030 (2010).
19. A. F. Fercher, W. Drexler, C. K. Hitzenberger, T. Lasser, "Optical coherence tomography—principles and applications," *Rep. Prog. Phys.* **66**, 239–303 (2003).
20. T.-W. Lo and P. Inderwiesen, "Fundamentals of seismic tomography," Society of Exploration Geophysicists, Tulsa, OK (1994).
21. A. J. Devaney, "Inverse-scattering theory within the Rytov approximation," *Opt. Lett.* **6**, 374–376 (1981).
22. J. Hebling, "Derivation of the pulse front tilt caused by angular dispersion," *Opt. Quan. Elec.* **28**, 1759–1763 (1996).